Semi-automated digital workflow to design and evaluate patient-specific mandibular reconstruction implants

van Kootwijk, A.; Moosabeiki, V.; Saldivar, M. Cruz; Pahlavani, H.; Leeflang, M. A.; Kazemivand Niar, S.; Tümer, N.; Mirzaali Mazandarani, M.; Zhou, J.; Zadpoor, A. A.

DOI
10.1016/j.jmbbm.2022.105291

Publication date
2022

Document Version
Final published version

Published in
Journal of the mechanical behavior of biomedical materials

journal of the mechanical behavior of biomedical materials 132 (2022) 105291

Contents lists available at ScienceDirect

Journal of the Mechanical Behavior of Biomedical Materials

journal homepage: www.elsevier.com/locate/jmbbm

Semi-automated digital workflow to design and evaluate patient-specific mandibular reconstruction implants

A. van Kootwijk [a], V. Moosabeiki [a,*], M. Cruz Saldivar [a], H. Pahlavani [a], M.A. Leeflang [a], S. Kazemivand Niar [b], P. Pellikaan [c], B.P. Jonker [d], S.M. Ahmadi [c], E.B. Wolvius [d], N. Tümer [a], M. J. Mirzaali [a], J. Zhou [a], A.A. Zadpoor [a]

[a] Department of Biomechanical Engineering, Faculty of Mechanical, Maritime and Materials Engineering, Delft University of Technology (TU Delft), Mekelweg 2, 2628 CD, Delft, the Netherlands
[b] Department of Mechanical Engineering, Tarbiat Modares University, Tehran, Iran
[c] Amber Implants BV, Prinses Margrietplantsoen 33, 2595 AM, The Hague, the Netherlands
[d] Department of Oral and Maxillofacial Surgery, Erasmus University Medical Center, Doctor Molewaterplein 40, 3015 GE, Rotterdam, the Netherlands

ARTICLE INFO

Keywords:
Mandibular reconstruction
Patient-specific implant
Implant design workflow
Topology optimization
Finite element analysis
Biomechanical validation

ABSTRACT

The reconstruction of large mandibular defects with optimal aesthetic and functional outcomes remains a major challenge for maxillofacial surgeons. The aim of this study was to design patient-specific mandibular reconstruction implants through a semi-automated digital workflow and to assess the effects of topology optimization on the biomechanical performance of the designed implants. By using the proposed workflow, a fully porous implant (LA-implant) and a topology-optimized implant (TO-implant) both made of Ti–6Al–4V ELI were designed and additively manufactured using selective laser melting. The mechanical performance of the implants was predicted by performing finite element analysis (FEA) and was experimentally assessed by conducting quasi-static and cyclic biomechanical tests. Digital image correlation (DIC) was used to validate the FE model by comparing the principal strains predicted by the FEM model with the measured distribution of the same type of strain. The numerical predictions were in good agreement with the DIC measurements and the predicted locations of specimen failure matched the actual ones. No statistically significant differences ($p < 0.05$) in the mean stiffness, mean ultimate load, or mean ultimate displacement were detected between the LA- and TO-implant groups. No implant failures were observed during quasi-static or cyclic testing under masticatory loads that were substantially higher (>1000 N) than the average maximum biting force of healthy individuals. Given its relatively lower weight (16.5%), higher porosity (17.4%), and much shorter design time (633.3%), the LA-implant is preferred for clinical application. This study clearly demonstrates the capability of the proposed workflow to develop patient-specific implants with high precision and superior mechanical performance, which will greatly facilitate cost- and time-effective pre-surgical planning and is expected to improve the surgical outcome.

1. Introduction

Mandibular reconstruction is a routine surgical procedure for the restoration of mandibular continuity defects, which typically result from tumor resection (benign or malignant), trauma, osteomyelitis, or osteoradionecrosis (Kumar et al., 2016; Goh et al., 2008; Wong et al., 2011). Patients with untreated defects may at a later stage suffer from facial deformity, loss of speech, and reduced masticatory function, which will severely affect the patient's quality of life (Wong et al., 2011). The ideal reconstruction procedure aims to optimize functional and cosmetic outcomes by restoring facial dimensions (*i.e.*, height, width, and projection), replacing compromised soft tissues, and providing a foundation for dental rehabilitation (Kumar et al., 2016). Even though the overall survival rate of free flap reconstructions is usually higher than 95%, there are several pivotal drawbacks associated with free tissue transfer, including the limited amount of available bone, donor site morbidity, and the need for high surgical expertise (Kakarala et al., 2018; W. B. Lee et al., 2018; Paré et al., 2019). Moreover, a large

* Corresponding author.
E-mail address: v.moosabeiki@tudelft.nl (V. Moosabeiki).

https://doi.org/10.1016/j.jmbbm.2022.105291
Received 11 March 2022; Received in revised form 18 May 2022; Accepted 19 May 2022
Available online 26 May 2022

variety of prostheses and osteosynthesis plates that are used for mandibular reconstruction have been reported to be associated with mechanical failure, usually resulting from premature fracture, loosening, or the exposure of either the implant itself or the screw fixation to the mandibular bone, as well as postoperative infections following wound dehiscence (Radwan and Mobarak, 2018; Seol et al., 2014). These complications often result in extended surgical procedures, prolonged hospital stays, long recovery processes, and an increased risk of surgical revisions (Vignesh et al., 2019).

Clinical studies on customized metallic implant reconstructions using a cage (or crib) design with or without the insertion of bone grafts have shown promising results (Kondo et al., 2015; W. B. Lee et al., 2018; Y.W. Lee et al., 2018; Malekpour et al., 2014; Mounir et al., 2020; Park et al., 2020; Rachmiel et al., 2017; Yamashita et al., 2008; Zhou et al., 2010). First, no or limited harvesting of autologous tissue is involved, minimizing the risk of associated donor site morbidity. Second, there is no need for intra-operative bending of the implant components, which decreases their susceptibility to fatigue fracture. Third, the procedure does not require additional surgical training or special experience. Finally, the natural configuration of the mandible can be accurately reproduced, leading to better aesthetics and patient satisfaction.

Tuning the shape and mechanical properties of the implanted material to match the patient's specific situation is deemed crucial for an optimal reconstruction and has been a driving force for the application of additive manufacturing (AM) technologies and computational tools, such as finite element analysis (FEA) to produce patient-specific implants (PSIs) (Oldhoff et al., 2021). Over the past few years, the use of topology optimization (TO) in the development of mandibular reconstruction implants has been increasing (Y.F. Liu et al., 2011; Y.F. Liu et al., 2017; C.H. Li et al., 2020). The optimization of the implant designs for orthopedic and craniofacial applications has resulted in improved success rates of the surgeries (Cheng et al., 2019). Yet, only a few studies have reported the details of the design process of the customized reconstruction implants, including the implementation of TO. Moreover, hardly any study has evaluated the performance of the designed implants under physiologically relevant loading conditions (Nasr et al., 2017). Consequently, a large variety of methodologies for implant design have been established, while standardized procedures regarding the design and testing of such implants have been lacking (Merema et al., 2021). This leads to unpredictable and incomparable results. Moreover, the labor-intensive nature of the involved processes means that the treatment workflow is expensive, inefficient, and time-consuming (León et al., 2020). There is, therefore, an urgent need for systematic and automated approaches to the design, fabrication, and (computational) testing of PSIs to pave the way for the integration of patient-specific cage-like reconstruction implants into routine care.

We, therefore, aimed to develop a semi-automated digital workflow for the design of patient-specific cage implants for mandibular reconstruction and to assess the effects of TO on the biomechanical performance of the implants through experimentally validated FEA models. The workflow proposed in this study was intended to help clinical engineers design reconstruction systems as a viable alternative to or in combination with the current standard free-flap approach in the treatment of mandibular continuity defects. Establishing a more systematic approach to the design of patient-specific mandibular reconstruction implants is expected to make pre-surgical planning more cost- and time-efficient while ensuring optimal aesthetics and minimizing morbidity. Furthermore, combining the design workflow with validated computational predictions regarding the implant performance provides a sound basis for the design decisions, leading to improved treatment outcome.

2. Materials and methods

The digital workflow starts with the post-processing of computed tomography (CT) scans (Fig. 1a–h) and runs towards a solid implant design (Fig. 2b), ready to be exported to the FEA software for TO. All image processing and implant designing steps were compiled into a Python-based semi-automated workflow using the Mimics Research 21.0 (Materialise, Belgium) and 3-matic 15.0 (Materialise, Belgium) Scripting Modules. All scripts were written to be compatible with Python version 3.8.

2.1. Bone model generation

A polyurethane (PU) mandible (Model 8950, Synbone AG, Switzerland) was scanned using a Siemens Somatom Volume Zoom CT scanner at a slice thickness of 0.6 mm, a peak potential of 140 kVp, and a field-of-view of 512 × 512 pixels (Fig. 1a). The segmentation and 3D

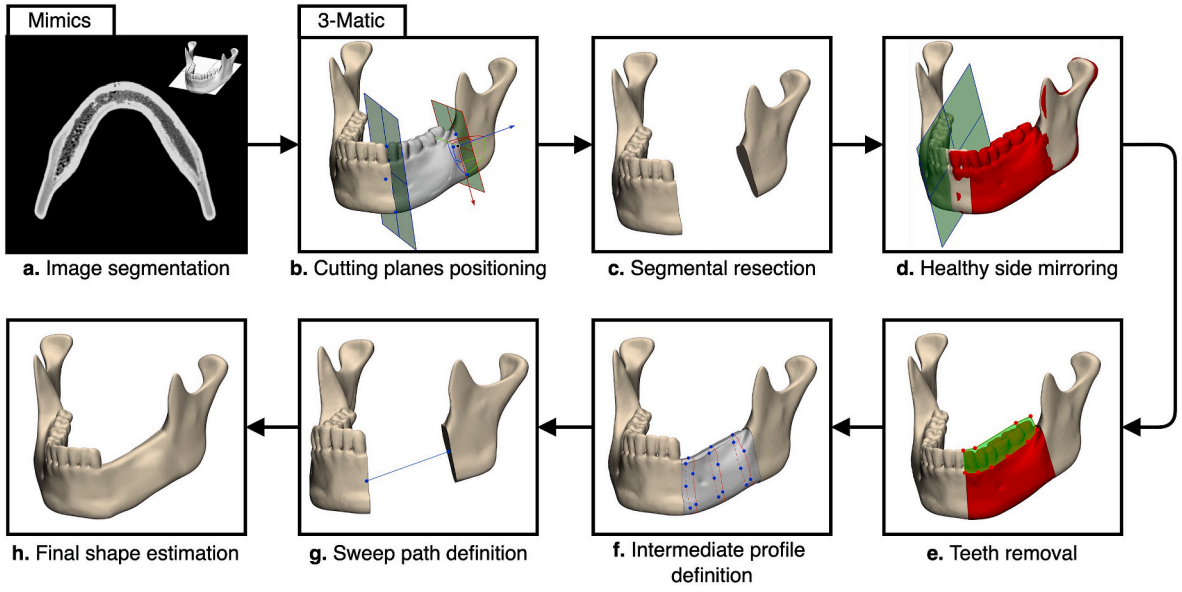

Fig. 1. The image processing step as well as the workflow for the estimation of the shape of the missing bone implemented in Mimics and 3-matic: (**a**) a horizontal plane viewport of the Synbone mandible reconstructed from the CT images, (**b**) the positioning of the osteotomy planes, (**c**) the segmental resection, (**d**) the mirroring of the healthy side onto the affected side, (**e**) the segmental cut-out and trimming of teeth, (**f**) the definition of intermediate contour profiles, (**g**) the definition of a centerline as a sweep path, and (**h**) the final result after performing the sweep-loft operation.

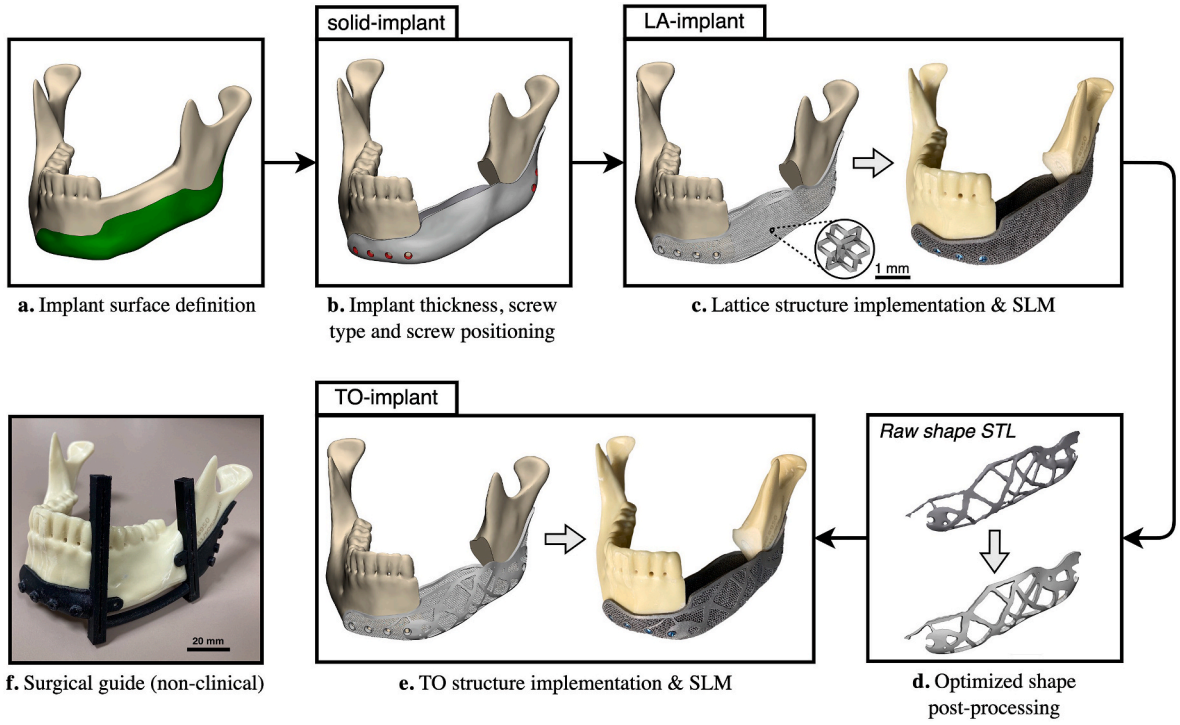

Fig. 2. The implant design workflow implemented in 3-matic: (**a**) implant surface marking, (**b**) implant thickness, screw type, and position definition, (**c**) the implementation of a dode-medium lattice structure in the virtual (left) and 3D-printed (right) LA-implant design after reconstruction, (**d**) the post-processing step of the TO body, (**e**) the implementation of the TO body to create the virtual (left) and 3D-printed (right) TO-implant design after reconstruction, and (**f**) non-clinical surgical guide.

part generation of the mandible were performed using Mimics Research 21.0 (Materialise, Belgium). The 3D mandible was then exported to 3-matic 15.0 (Materialise, Belgium) where resection, missing bone shape estimation, and implant designing procedures were carried out.

The resection area investigated in this study was a 4-cm long lateral defect that ranged from the canine tooth up to the mandibular angle (Fig. 1c). The reason for choosing this area was that a lateral defect type (*i.e.,* between the mandibular condyle and symphysis) corresponds to the region that is most frequently subjected to resection during the surgical treatment of advanced squamous cell carcinomas (Coletti et al., 2009; Doty et al., 2004; Ettl et al., 2010; Gutwald et al., 2017; Shibahara et al., 2002). The osteotomy planes for resection were defined by positioning two datum planes (Fig. 1b).

A combination of the segmental mirroring technique and anatomical extrusion technique was implemented in the current design workflow for shape estimation (Khalifa et al., 2016; Moiduddin et al., 2016). First, the intact side was mirrored across the midsagittal plane onto the affected side (Fig. 1d). Next, the missing segment was cut out of the mirrored side between the previously defined osteotomy planes, and teeth were trimmed off (Fig. 1e). Three curves were then created around the surface of the mirrored segment, which served as intermediate contour profiles for the "sweep" operation (Fig. 1f). A centerline was created between the two boundary surfaces of the remaining mandibular segments to provide a path for the sweep operation (Fig. 1g). The estimated shape was generated by using a sweep-loft operation from one resection margin to the other, following the sweep path and the intermediate contour profiles (Fig. 1h).

2.2. Implant designing

Two different implant designs were investigated in this study: a fully porous implant based on a lattice structure (*LA-implant*) and a topology-optimized design (*TO-implant*). A non-porous design (*solid-implant*) was used for the TO procedure.

The implant design procedure in 3-matic starts off by marking the manifold on the mandible that defines the outer shape of the implant (Fig. 2a). An implant thickness of 1.5 mm was set to create the solid implant (Fig. 2b). The general shape of the implant follows the contour of a cage or a tray. The implant height in the resected area was defined to be slightly smaller than the native mandible so that the implant can be covered with sufficient soft tissue without the need for an additional local flap (Qassemyar et al., 2017). Yet, the cage was designed with a sufficient height to allow for any required dental implants to be positioned atop the integrated bone graft at a later stage to restore masticatory performance. Then, the screw sizes (length and diameter) and screw positions were defined: eight 2.4 mm bicortical titanium cortex screws (MatrixMANDIBLE, DePuy Synthes, USA) were used to fixate each of the implants to the mandible. Four screws were placed on the anterior body and another four on the posterior lateral border of the ramus (Fig. 2b). The four screws placed in the chin region were 14 mm long. Both screws on the posterior mandibular segment closest to the resection border were 8 mm long. The most distal screws on the posterior mandibular segment were both 6 mm long.

A proper design of the porous structure is crucial for promoting osseointegration and angiogenesis, reducing implant stiffness, and disrupting fibrosis (Koschwanez and Reichert, 2013). Lattice structures based on the 'dode' unit cell were used to implement porosity in the solid implant, as previous studies have found them to be promising (Moiduddin et al., 2019; Moiduddin et al., 2020). The implementation of the lattice structures was carried out using Magics 24.01 (Materialise, Belgium). Three default dode unit cell structures were initially considered, namely, 'dode-thin', 'dode-medium', and 'dode-thick' with stepwise increases in the strut thickness. The implant with the dode-thin structure resulted in a very high porosity (96%), a small strut thickness (110 μm), and poor strut connections, which would lead to a fragile implant with insufficient mechanical strength. The dode-medium and dode-thick unit cell structures met the design requirements, including a minimum pore size of 400 μm with a porosity of 70–90%, which are

suggested to be optimal for bone regeneration (Bobbert and Zadpoor, 2017; Wang et al., 2017)). 3D printed implant samples with both unit cell structures showed that the permeability of the dode-thick lattice structure was impeded in various regions due to the fusion of powder particles in-between the struts. Hence, the 1.5-mm dode-medium unit cell (Fig. 2c zoom-in) was selected for the lattice structure in the final implant design. These unit cells had an in-plane pore size, strut thickness, and porosity of 460 μm, 210 μm, and 87.5%, respectively.

The LA-implant was entirely porous (Fig. 2c) except for the solid edges around the screw holes and the implant extremities, which were maintained to provide the implant with additional mechanical strength and to protect the surrounding tissue from sharp strut ends. The topology optimized design resulting from the TO analysis was exported out of Abaqus as a raw STL part and was post-processed in 3-matic (Fig. 2d) by reproducing this shape from the solid implant with a consistent thickness. The TO-implant (Fig. 2e) was then obtained by combining the TO volume with the porous LA-implant through Boolean unification, as described by Peng et al. (2021). More details on TO are provided in Subsection 2.3.4.

2.3. FEA methods

All FE analyses were performed using Abaqus/CAE 2019 (Simulia, Dassault Systèmes, France). The TO was performed using Abaqus/CAE 2017 (Simulia, Dassault Systèmes, France). Before a complex musculatory system was implemented in the FE model, a simplified model that reproduced the experimental conditions (*EXP-FEA*) was developed. By doing so, two validation steps were integrated into the FEA process. First, the *EXP-FEA* model was validated against the experimental data. Afterwards, this model was extended to include more sophisticated physiological conditions (*PHY-FEA*), thereby simulating the clinical situation. The results of the *PHY-FEA* model were then compared with the FEA data published in the literature. The healthy intact mandible was used for the validation of the *EXP-FEA* model using the digital image correlation (DIC) technique (see Section 2.5). Four different models were investigated under the *PHY-FEA* conditions, respectively representing the healthy intact mandible (*healthy-model*), the resected mandible model with the solid implant (*solid-implant-model*), the resected mandible model with the LA-implant (*LA-implant-model*), and the resected mandible model with the TO-implant (*TO-implant-model*) (Table 1).

2.3.1. Material assignment

In the case of *EXP-FEA*, the material properties were homogenously assigned to the cancellous and cortical regions of the mandible. A negligible Young's modulus [E] of 1×10^{-6} GPa was assigned to the cancellous bone region, given that it does not significantly contribute to the stress distribution in the implant (Koper et al., 2021). The Young's modulus of the cortical bone region was chosen such that the stiffness of the model would match the stiffness derived from the experimental data. By using this approach, a Young's modulus of 0.41 GPa was found for the cortical PU region (see subsection 3.1). The Poisson's ratio was set at $\nu = 0.3$.

In the case of *PHY-FEA*, the cancellous bone and cortical bone regions were respectively defined as those corresponding to $HU < 620$ and $HU > 620$, where HU is the Hounsfield unit. The empirical relationship between the density and elastic modulus of mandibular bone are available in the literature (Ay et al., 2016) and will be used in actual clinical use of the workflow. In the present study, however, we had to work with the HU values of the synthetic mandible, which are different from those of the real mandibular bone. The density-modulus relationships, therefore, had to be adjusted to obtain values that would match the average values of density [ρ] and elastic modulus [E] of the actual mandibular bone. For cancellous bone, the material properties were calculated using the following equations:

$$\rho = 5 + 0.005HU \quad (1)$$

$$E = 0.06 + 0.9\rho^2 \quad (2)$$

This resulted in ρ-values ranging between 0.08 and 1.70 g/cm^3 and E-values ranging between 0.07 and 2.67 GPa. For the cortical bone, the material properties were calculated using the following equations:

$$\rho = 2.7 + 0.00165HU \quad (3)$$

$$E = 0.09 + 0.9\rho^{4.3} \quad (4)$$

This resulted in ρ-values ranging between 1.73 and 2.67 g/cm^3 and E-values ranging from 9.61 to 43.46 GPa. The elastic modulus of the outer voxel layer was set to $E = 30.1$ GPa, which corresponds to the average elastic modulus of the dentulous mandibular cortex as determined by Ay et al. (2016), to avoid the issues related to the partial volume effect. The volume mesh of the healthy model and the corresponding material assignment are presented in Fig. 3b and c. A similar process was followed in the case of the implanted mandibles. The implants, made of the Ti–6Al–4V ELI alloy, were assigned with an elastic modulus of 120 GPa (SLM Solutions, Material Data Sheet). A Poisson's ratio of 0.3 was assigned to all the volume elements of both the mandible and implant. All materials were modeled as linear elastic and isotropic.

2.3.2. Meshing

The mandible and implants (LA-implant and TO-implant) were discretized using 4-node tetrahedral elements (C3D4) and 10-node quadratic (C3D10) elements, respectively (Fig. 3a). A mesh convergence study was performed to define the element sizes. Accordingly, the mandible and implants were discretized using ≈700,000 and ≈3,500,000 elements, respectively. For TO, the solid implant was discretized using ≈200,000 C3D4 elements.

Table 1
The study design for FEA modeling and experimental testing.

		FEA			Experimental testing				
		EXP-FEA	PHY-FEA		Quasi-static			Cyclic	
								Constant-cyclic-method	Increment-cyclic-method
Loading condition		INC (I[a])	INC (II[a])	RMB (II)	INC (I)	INC (II)	RMB (II)	INC (I)	INC (I)
Sample	Control[b]	EXP-FEA model	healthy-model		1[c]	2	2	–	–
	Solid implant	–	solid-implant-model		–	–	–	–	–
	LA implant	–	LA-implant-model		–	3	3	2	2
	TO implant	–	TO-implant-model		–	3	3	2	2

Numbers in the column "Experimental testing" indicate the number of the specimens used.

[a] 'I' indicates a 50%/50% healthy side/affected side load distribution while 'II' indicates a 70%/30% healthy side/affected side load distribution. INC: incisal clenching; RMB: right molar biting.

[b] The control specimens represent the intact (non-implanted) mandibles.

[c] This control specimen was used for the DIC measurement.

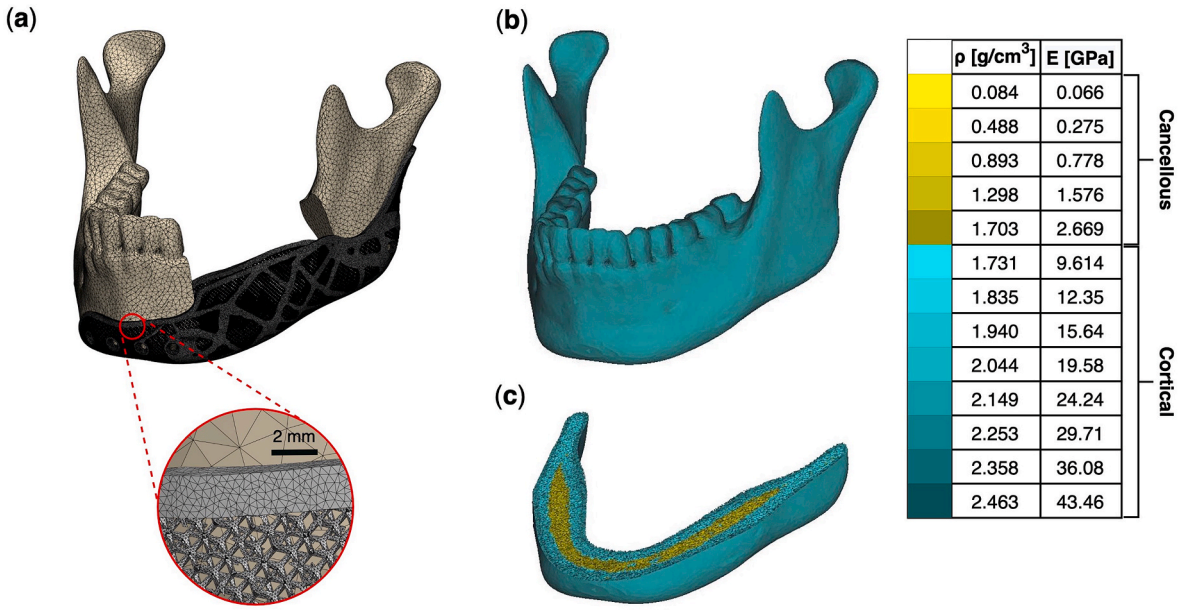

Fig. 3. (**a**) An overview of the surface mesh applied to the mandible and TO-implant in the TO-implant-model, (**b**) the full and (**c**) cross-sectional views of the material assignment to the volume mesh of the healthy-model. The color scale represents the corresponding values of the density and Young's modulus calculated for the cortical and cancellous regions of the mandible shown in (b) and (c).

2.3.3. Loads and boundary conditions

The loads and boundary conditions applied in the *EXP-FEA* model closely resembled those of the experimental setup (Fig. 4a). The steel loading bar was modeled as an undeformable rigid object, given its high stiffness as compared to the PU bone specimen. It exerted an equal force on both sides of the mandible by displacing it 5 mm in the positive *z*-(*i.e.*, superior) direction while constraining all the other possible translations and rotations (Fig. 4b). This displacement was enough to capture the linear part of the load-displacement curve obtained from the biomechanical experiments. Only incisal clenching (INC) of the jaw was evaluated in the *EXP-FEA* model. This was done by restraining the incisal surfaces of the central and lateral incisors from moving vertically (*i.e.,* perpendicularly to the occlusal plane) while restraining the movement of the articular surface of the temporomandibular joints in all directions. A friction coefficient of 0.2 was used at the interface of the bar and the bone.

Two types of clenching movements were simulated using the four models of the *PHY-FEA* group, including INC and right molar biting (RMB) at the unaffected side (Fig. 4c). The same boundary conditions as described for *EXP-FEA* were used to create the INC condition. For RMB, the occlusal surfaces of the first and second molar were restrained from moving vertically while restraining all the possible movements of the articular surface of the temporomandibular joints.

Four different muscles (masseter, temporalis, medial pterygoid, and lateral pterygoid) were modeled bilaterally through three-dimensional force vectors (Pinheiro and Alves, 2015). In the case of the healthy mandible, all four muscles were used bilaterally to create the required loading conditions. For some segmental resections, muscles can be (partially) reattached to the mandible, which can then continue to perform their function after implantation (to a limited extent). The residual muscle force after mandibular reconstruction is reported to be 60% of the average biting force of healthy adults (Moghaddam et al.,

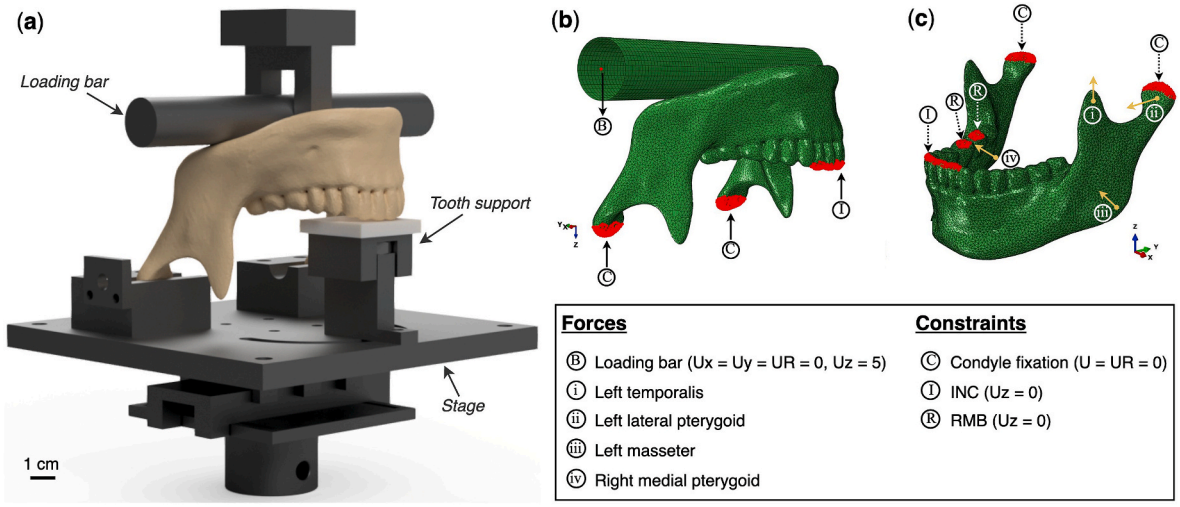

Fig. 4. (**a**) The experimental setup, (**b**) the displacement (U) and rotation (UR) constraints in the *EXP-FEA* model, and (**c**) the constraints and resultant muscle force directions for the incisal clenching (INC) and right molar biting (RMB) conditions in the *PHY-FEA* group. For simplicity, the muscle force vectors are only partially shown on the left and right sides of the mandible.

2016). The implant used in this study covered an area on the posterior mandibular segment that made the reattachment of both the left masseter and the left medial pterygoid unlikely. Therefore, the forces exerted by these muscles were excluded from the loading conditions in the solid-implant-model, LA-implant-model, and TO-implant-model.

Pinheiro and Alves (2015) have described the expected reaction forces on the teeth involved in INC (570.90 N) and RBM (600.40 N). These forces were based on the average maximum single-tooth bite forces of young male adults. In the present study, the residual muscle force may be lower than 60% of the original maximum muscle force because two of the muscles are not going to be reattached to the affected side of the mandible. Since the exact reduction in the muscle forces could not be estimated, a general 'worst-case' scenario was simulated to ensure a good mechanical performance of the implant in the long term. To this end, the maximum biting forces described above were reduced by 40% as described by Moghaddam et al. (2016). This resulted in the reaction forces of 342.54 and 360.24 N during INC and RMB, respectively. All individual muscle forces were scaled, depending on the desired biting conditions. The weighting factors of each muscle, the orthogonal directions, and the scaling factors that provided the muscle activation force are specified by Korioth and Hannam (1994) and are later adapted by Pinheiro and Alves (2015). The mandible models in this study were aligned with the reference frame used by Pinheiro and Alves, according to the cephalometric standards. The muscle forces could, therefore, be simply scaled uniformly until the teeth were subjected to the desired magnitude of reaction forces. For INC and RMB, those scaling factors were 0.72 and 0.87, respectively. The displacement patterns in the healthy-model were compared with the displacements obtained by Korioth and Hannam (1994). The three-dimensional force vectors of each muscle group for both loading cases, as well as the number of the nodes to represent each muscle group are listed in Table S.1 (Supplementary material) for the healthy-model and in Table S2 (Supplementary material) for the implanted models.

2.3.4. Topology optimization

The Abaqus Topology Optimization Module was used for the TO of the solid implant. Maximizing open space in the implant is beneficial for the healing process of the graft. Taking this and the benefits of implant weight reduction into account, the optimization constraint was set to constrain the final TO implant volume to 10% of the initial solid implant volume. The objective function was set to minimize the compliance of the system. Since the global shape of the implant had been defined earlier, no geometrical restrictions were applied to the optimization procedure.

2.4. Experimental methods

Ten LA-implants and ten TO-implants were 3D printed using grade 23 Ti–6Al–4V ELI powder. A selective laser melting (SLM) machine (SLM Solutions Group AG, Germany) was used. The chemical composition of the titanium alloy powder is listed in Table S3 (Supplementary material). The main SLM process parameters, powder particle sizes, and the physical properties of the as-built material are presented in Table S4 (Supplementary material). All the implanted specimens were prepared by using a customized surgical cutting and drilling guide (Fig. 2f) to create nearly identical resections and screw holes in each mandible. Note that the surgical guide was not designed to be suitable for intra-operative clinical application. The screw holes were predrilled using a 1.8-mm drill bit and the resection area was cut out using an oscillating saw. The experimental test setup (Fig. 4a) was designed both for quasi-static testing using a Lloyd Instruments LR5K testing machine and for cyclic fatigue testing using an INSTRON ElectroPuls™ E10000 machine. In order to create a specific clenching task, a distributed load was applied to both mandibular angles by means of a rigid seesaw device while fixing the translations of both condyles and constraining a certain region on the dental arch perpendicular to the plane of occlusion. Only the rotational movement of the condyles about the transverse horizontal axis was allowed. Several translational and rotational degrees of freedom were implemented in the designed fixture to enable the evaluation of the implant performance under various biting conditions, including INC and RMB. To enable an accurate comparison between the numerical and experimental results, the mandibles were positioned according to the cephalometric standards with their inferior border positioned at an angle of 26° with respect to the horizontal plane (Gateno et al., 2013).

2.4.1. Quasi-static testing protocol

During both INC (Fig. 5a) and RMB (Figs. 5b), 70% and 30% of the load were applied to the mandibular angles of the healthy and affected sides, respectively (Gateno et al., 2013; Rendenbach et al., 2017; Schupp et al., 2007). Three LA-implant samples, three TO-implant samples, and two control specimens (*i.e.*, intact non-implanted mandibles) were tested in these two groups (Table 1). The specimens were subjected to continuous compressive loading at a rate of 1 mm/min until the specimen failed, which was defined as the fracture of the plate or mandible, failure at the screw-substrate interface, or a vertical displacement above 20 mm. A preload was set at 10 N (Koper et al., 2021). For each sample, the failure or ultimate load (U. load) [N] of the construct, ultimate displacement (U. displacement) [mm], and the location of failure were recorded. The construct stiffness [N/mm] was determined from the slope of the best-fit line in the linear portion of the load-displacement curve. The one sample *t*-test with Bonferroni correction was used to determine the differences between both implant groups. $p < 0.05$ was set as the threshold of statistical significance.

2.4.2. Cyclic testing protocol

The cyclic testing setup is shown in Fig. 5c. A 50%/50% INC loading configuration was used as this yielded the most stable setup while transferring the highest load through the implant. First, the fatigue performance of the implant was evaluated under physiological conditions (*constant-cyclic-method*) by cycling the stress over a constant range between the minimum (30 N) and maximum (340 N) compressive stresses (Fig. 5e). The reconstruction system must survive up to a maximum of 250,000 loading cycles under this post-surgical 'worst-case' loading condition to guarantee the long-term mechanical function of the implant (Gutwald et al., 2017; Schupp et al., 2007). To detect any potential implant failures or screw loosening due to fatigue under higher loads, a second cyclic testing procedure (*increment-cyclic-method*) was used (Fig. 5f). In this procedure, the maximum stress amplitude was increased incrementally (3 N per cycle) from the initial load of 340 N until the failure of the implant sample or until a maximum load of 2500 N was reached. For the tests with each of the two cyclic testing methods, four reconstructed samples were tested of which two contained the LA-implant and two contained the TO-implant (Table 1). The loading rate was set at 3 Hz (Gutwald et al., 2017; Schupp et al., 2007). The number of cycles to failure and the failure load were registered.

2.5. DIC measurements

A Q-400 2x12MPixel digital image correlation (DIC) system (LIMESS GmbH, Krefeld, Germany) was used to measure the surface strains on the intact mandible during quasi-static testing employing an imaging frequency of 1 Hz. The posterior segment of the mandible, corresponding to the implanted side in the case of the implanted mandibles, was selected as the area of interest, as it included the primary location of the specimen failure. A black dot speckle pattern was applied over a white paint background to cover the entire area of interest. Two digital cameras and light emitting diode (LED) panels were placed at 0.8 m from the specimens to capture their images and illuminate them, respectively (Fig. 5d). Image processing and strain calculations were performed using Istra4D x64 4.6.5 (Dantec Dynamics A/S, Skovunde, Denmark). Two enclosed polygonal regions, denoted as Polygon_1 and Polygon_2, were created

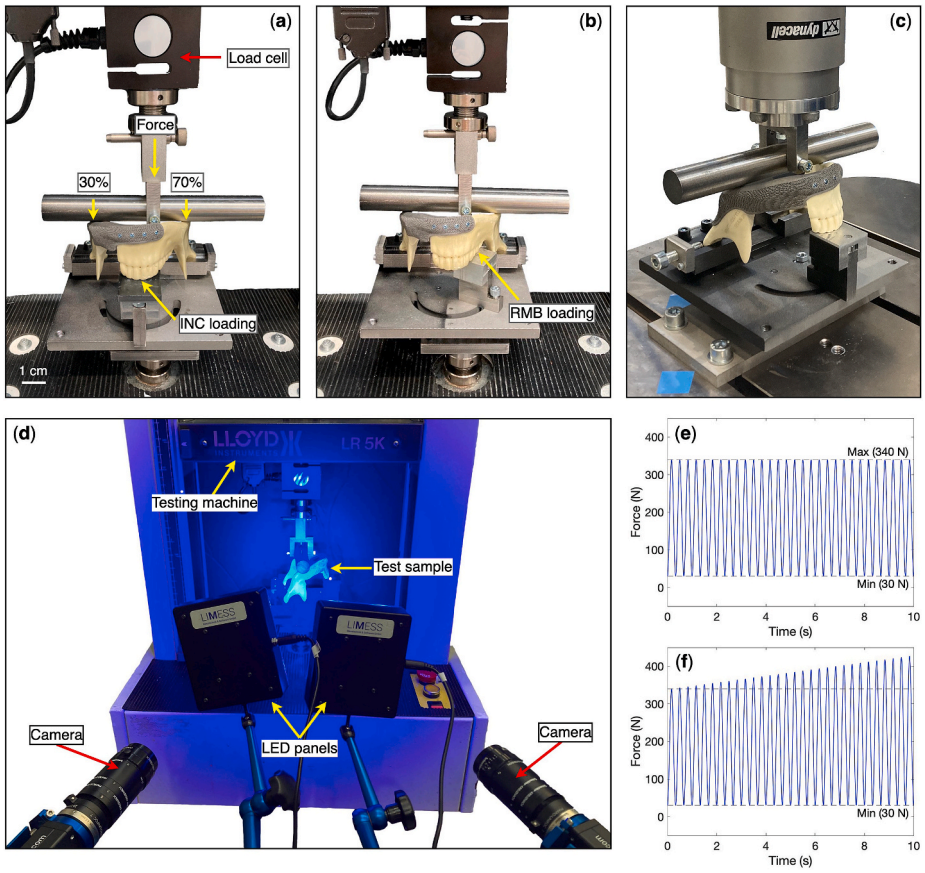

Fig. 5. Quasi-static (**a**) INC and (**b**) RMB loading setup using a 70%/30% force distribution. (**c**) The cyclic testing setup using a 50%/50% force distribution. (**d**) The experimental setup for DIC measurements. The cyclic loading sine waves plotted against the applied force during the first 10 s of the cyclic tests with (**e**) the constant-cyclic-method and (**f**) the increment-cyclic-method.

Table 2
The results of the cyclic tests performed using the increment-cyclic-method.

Group	Sample	# Cycles to failure	Failure load [N]
LA-implant	1	501	1820
LA-implant	2	594	2099
TO-implant	1	579	2033
TO-implant	2	448	1647

Table 3
A comparison between the design outcomes and mechanical performances of the LA- and TO implants.

	LA-implant	TO-implant[a]
Design outcomes		
Implant weight [g]	15.8	18.4 (+16.5%)
Implant porosity [%]	63.4	52.4 (−17.4%)
Estimated workflow time [h]	3	22 (+633.3%)
Mechanical performance[b]		
Implant failure (static or fatigue)	No	No
Screw loosening (static or fatigue)	No	No
Mean construct stiffness [N/mm]	311.5 ± 8.3	323.3 ± 21.9 (+3.8%)
Mean ultimate load [N]	1200.9 ± 54.0	1271.5 ± 112.0 (+5.9%)
Mean ultimate displacement [mm]	5.3 ± 0.3	4.9 ± 0.4 (−7.5%)

[a] The values between brackets indicate the percentage of change with respect to the LA-implant.
[b] The values of the mean construct stiffness, mean ultimate load, and mean ultimate displacement are presented for the INC 70%/30% loading condition.

within the anterior and posterior condylar neck regions of the mandibular bone, corresponding to the areas of the largest maximum and minimum principal strains, respectively. The mean strain values in each of these two areas were extracted and plotted against the applied force. Similarly, both corresponding areas, denoted as Area_1 and Area_2, were identified in the FE model, and the average nodal strain values in both areas were plotted against the reaction force on the loading bar (Fig. 4a). Only the linear elastic portion of the applied force was used for comparison with the DIC data, as plasticity was not considered in our FE analyses.

3. Results

3.1. FEA results

In *EXP-FEA*, the computational value of the stiffness (278.5 N/mm) agreed with the experimental value obtained using quasi-static testing (274.9 N/mm) (Fig. 6d) when a Young's modulus of 0.41 GPa was assigned to the cortical PU region. Fig. 6a shows the von Mises stress distribution within the intact mandible for a load of 800 N. The highest stress values were found at the posterior (12 MPa left and 16 MPa right) and anterior sides (14 MPa left and 16 MPa right) of the condylar neck, as well as along the external oblique line (8 MPa left and 9 MPa right). The deformations of the mandible as predicted by the *EXP-FEA* model (up to 1375 N) and as measured using the quasi-static experiments (up to fracture) are presented side by side in Video S.1 (animation in the supplementary material).

Supplementary video related to this article can be found at https://doi.org/10.1016/j.jmbbm.2022.105291

The distributions of the maximum and minimum principal strain

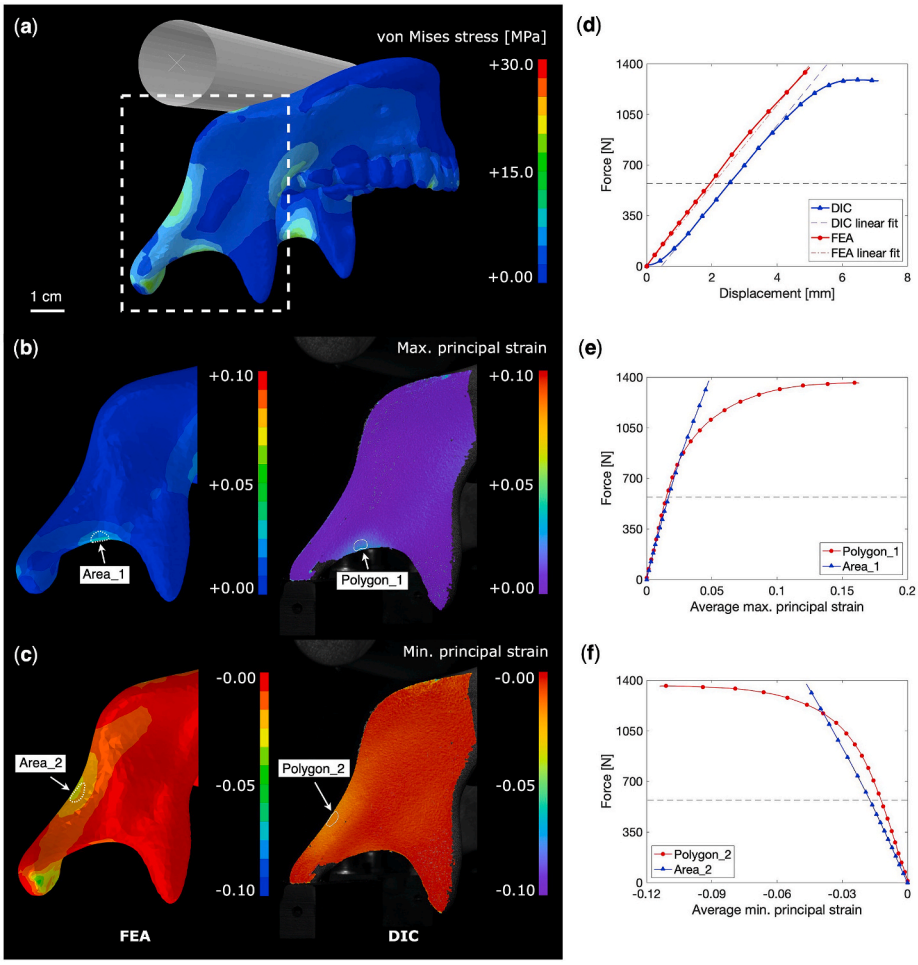

Fig. 6. (**a**) The contour of the von Mises stress [MPa] within the intact mandible as predicted by the *EXP-FEA* model (800 N). (**b**) A comparison of the maximum principal strains within the intact mandible as obtained by the FEA model and DIC measurements. (**c**) A comparison between the minimum principal strains within the intact mandible predicted by the FEA model and the experimental values measured using DIC. The strain fields correspond to a load of 800 N. (**d**) The computational and experimental force-displacement curves of the intact mandible. The dotted and dashed lines represent the best-fit approximations of the linear portion of the curves. (**e**) The mean values of the maximum principal strain extracted from the surfaces in Area_1 and Polygon_1. (**f**) The mean values of the minimum principal strain extracted from the surfaces in Area_2 and Polygon_2. The horizontal dashed lines in (d–f) indicate the mean values of the maximum biting force of healthy individuals.

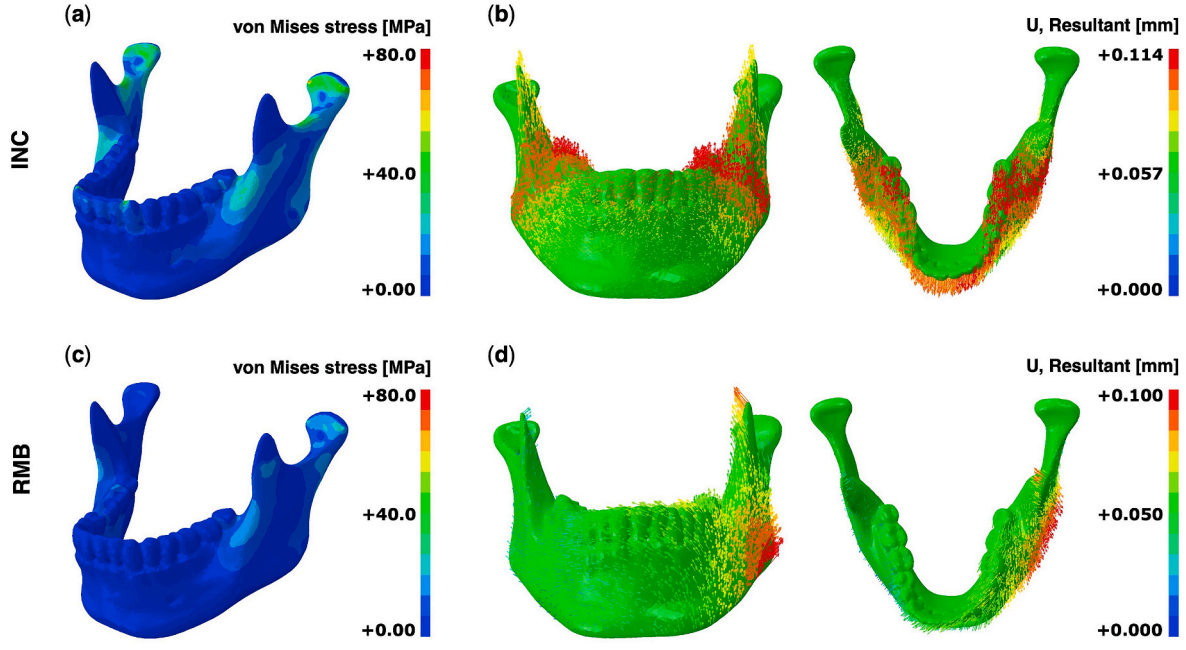

Fig. 7. (**a**) The distribution of the von Mises stresses [MPa] and (**b**) the resulting deformation U [mm] in the healthy-model under the INC condition. (**c**) The distribution of the von Mises stresses [MPa] and (**d**) the resulting deformation U [mm] in the healthy-model under the RMB condition. The maximum deformations in (b) and (d) are magnified 50 times. Arrows in the vector plots represent the total displacement of each node. The color and length of the arrows indicate the magnitude and direction of the displacements, respectively.

predicted by the FEA models and measured by DIC (load = 800 N) are presented in Fig. 6b and c, respectively. The means values of the maximum and minimum principal strains in the regions of interest were plotted against the applied force (Fig. 6e and f, respectively). In the linear elastic range (*i.e.*, between 150 and 850 N), the maximum principal strains measured by DIC within Polygon_1 were in good agreement with the strains predicted by the FE model within Area_1. The minimum principal strains in both regions were linearly correlated but slightly higher in Area_2 as compared to Polygon_2, with a difference of 31% at 800 N.

In *PHY-FEA* (healthy-model), the combined muscle forces resulted in the biting forces of 570.9 and 600.4 N during INC and RMB, respectively. The distributions of the von Mises stress within the healthy mandible subjected to the INC and RMB loading are presented in Fig. 7a and c, respectively. Similar to Pinheiro and Alves's results (2015), the high stresses under INC loading were observed below the condylar process in the mandibular notch (37 MPa), along the external oblique line (29 MPa), and at the posterior surface of the ramus (33 MPa). Consistent with the findings of Pinheiro and Alves (2015), the high stresses under the RMB loading were found on the posterior surface of the contralateral ramus, when compared with the working (right) side, as well as along the external oblique lines on both sides.

The deformations in the healthy-model under INC and RMB loading are presented in Fig. 7b and d, respectively. Under INC, most deformations occurred around the dental arch. The overall deformation patterns were very similar to those obtained by Korioth and Hannam (1994) with the molars moving up and slightly inward and the front teeth moving forward. The results corresponding to the RMB case agreed with the Korioth and Hannam's results too, including a counterclockwise torsional movement with a maximum deformation that was located at the left gonial angle.

Fig. 8 shows the distribution of the von Mises stresses in the solid-implant-model, LA-implant-model, and TO-implant-model under the INC and RMB conditions. For all the three models, the stresses on the mandibular bone were mainly located on the anterior and posterior condylar neck and on the external oblique line of the contralateral side during INC and on the condylar neck of the lateral side during RMB. During both INC and RMB, the stresses around the contralateral condyle were similar in the three models (around 40 MPa), whereas the stresses on the lateral condyle were lower in the solid-implant-model (15 MPa for RMB) as compared to the TO-implant-model (23 MPa for RMB) and lattice-implant-model (55 MPa for RMB). The stress concentrations in the bone were noted in and around the first and second screw holes closest to the posterior resection margin, with a maximum value of 36 MPa observed in the TO-implant-model. The maximum von Mises stresses in the mandible bone in all the models were well below the mean compressive yield strengths of the cortical mandibular bone, which are reported to be 200, 110, and 100 MPa along the longitudinal, tangential, and radial directions, respectively (van Eijden, 2000).

The von Mises stresses inside the implants were higher under the RMB condition as compared to the INC condition in all the three implant reconstruction models. Some elevated stresses occurred around the anterior screw holes but the highest stress values were concentrated around the first posterior screw hole near the resection and to a lesser extent along the curved implant edge above that screw. The magnified views at the bottom of Fig. 8 show that the elevated stress values in these critical areas during RMB stayed well below the yield strength of Ti–6Al–4V (*i.e.*, 800 MPa) (Li et al., 2020).

3.2. Experimental testing results

The weights of the LA-implant and TO-implant after 3D printing were 15.8 and 18.4 g, respectively. These values are considerably lower than those of the implants used in previous studies (*e.g.,* implants with an average weight of 60 g in a study by Mounir et al. (2020)). No problems were encountered during the preparation of the specimens.

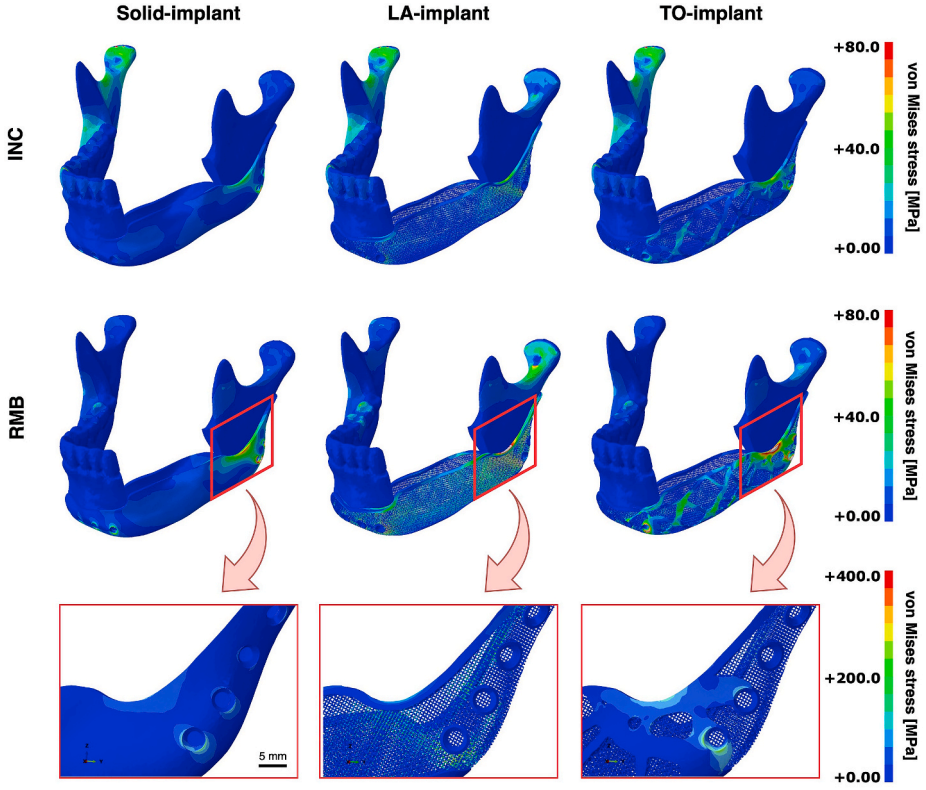

Fig. 8. The distributions of the von Mises stresses [MPa] in the three implant models under the INC (top) and RMB (middle) conditions. The magnified views (bottom) illustrate the stress concentrations across the lateral mandibular angle region under the RMB condition.

For all the specimens, excellent fit was obtained between the implant and the remaining mandibular segments, and tight screw fixation was established after the preparation of the samples using the surgical guide (Fig. 2f).

Implant failure or failures at the screw-substrate interface were not observed in any of the samples during the quasi-static biomechanical testing. The force-displacement graphs for the INC and RMB loading conditions are presented in Fig. 9a and b, respectively. The fracture occurred in the condylar neck region in all the cases, either on the implanted side or on the intact side, depending on the loading condition. In all the cases, the fracture occurred for loads (>1000 N) far above the maximum physiological biting force of healthy individuals (570.9 N during INC and 600.4 N during RMB). This provides the implant with a substantial safety margin in terms of the maximal loads that the reconstructed system can bear in the case of clinical application.

The stiffness, ultimate load, and ultimate displacement of the specimens are presented as grouped scatter plots in Fig. 9c, d, and 9e, respectively. The intact mandibles and both implant designs exhibited comparable mechanical stiffness, ultimate loads, and ultimate displacements during the tests. No significant differences ($p < 0.05$) were found between the groups under INC and RMB loading conditions.

All the cyclic tests of the specimens that were performed using the constant-cyclic-method ran their course up to the maximum number of cycles without any signs of bone failure, implant failure, or any visible changes in the screw fixations. During the subsequent removal of the implants, none of the screws were found to be loose. As for the tests with the increment-cyclic-method, no implant failures, or failures at the screw-substrate interface were observed. The number of cycles to failure and the failure load acting on each of the four samples are listed in Table 2. Similar to the quasi-static tests, the specimens tested using the increment-cyclic-method fractured in the condylar neck region of the mandible (three out of four specimens). One exception was identified (TO-implant, sample 2 in Table 2) where the mandible fractured in the region of the external oblique line and anterior mandibular angle.

The low von Mises stresses observed in the solid implant (Fig. 8) indicate that the solid implant could perform well in the sense that no implant fractures are expected to occur under the applied loads. Yet, no experimental tests of the solid-implant-model were performed, as it was not considered suitable for clinical application. Its high stiffness and complete absence of implant permeability would almost certainly lead to the atrophy of the bone graft, thereby significantly reducing the implant longevity. Therefore, the main comparison in terms of the implant performance was performed between the LA and TO implant groups. Table 3 lists the most important findings of the study to enable a direct comparison between both design approaches.

4. Discussion

We developed a digital workflow for the design of patient-specific implants to restore lateral mandibular defects. Using this workflow, two proof-of-concept cage-shaped implants were designed to match the anatomy of a laterally resected synthetic mandible phantom. While one of the designed implants was fully porous, the other was topology-optimized. The excellent match between the screws and implant on the one hand and between the implant and the mandibular segments on the other confirms the capability of the developed workflow to design customized implants with accurate dimensions. The computationally predicted strains agreed with the DIC measurements. Moreover, the observed locations of specimen failure coincided with the computationally predicted ones. These observations confirm the reliability of the computational models. For both implant designs, the overall implant stresses under post-surgical chewing conditions stayed well below the yield stress of Ti–6Al–4V. Neither the implants nor screw-substrate fixations failed during the quasi-static or cyclic tests, meaning that the strengths of both implants exceeded the strengths needed to withstand the mean maximum bite forces experienced after mandibular resection. The comparison between both types of implants indicated that the fully porous implant may be preferable to the topology-optimized one as it offers a lower weight, a higher porosity, and a shorter design time.

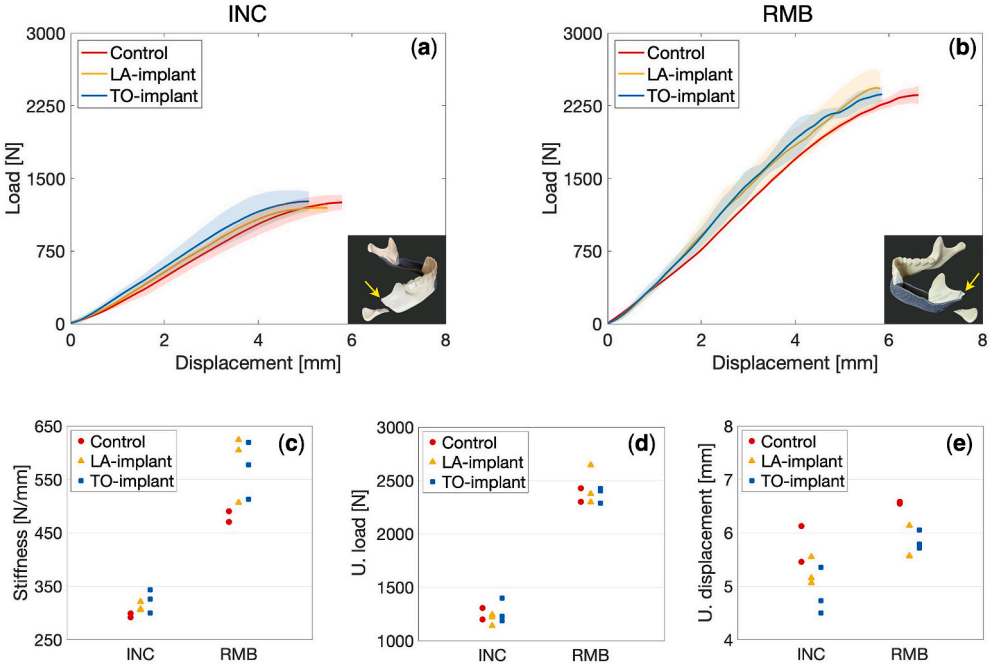

Fig. 9. The load-displacement curves obtained from the quasi-static tests under the (**a**) INC and (**b**) RMB loading conditions. For each group, the lines and shaded areas indicate the mean and standard deviation, respectively. The small inset images on the bottom right indicate the fracture location in each group. The grouped scatter plots of the stiffness (**c**), ultimate load (**d**), and ultimate displacement (**e**) of the constructs. The control specimens represent the intact (non-implanted) mandibles.

4.1. Image processing, shape estimation and implant designing

The software used for each of the processes in the current workflow (*i.e.,* image processing and implant designing) allows for the customization of their graphic user interface (GUI) through Python scripting. Abaqus/CAE offers a Python-based GUI toolkit too, making it possible to couple the design workflow with an FEA-plugin in the near future.

The segmental mirroring of the mandible in combination with a "sweep" operation was the method of choice to estimate the shape of the missing part of the mandible after resection. Statistical shape models (SSM) can be considered as an alternative to estimate the missing bone shape. An advantage of using the mirroring technique compared to SSM is that no additional database with training samples is required, which makes the procedure easier to implement in the workflow. However, mirroring is not possible if both sides of the mandible are affected. For example, the mirroring technique is not applicable to central defects or lesions that cross the midline. Moreover, the presence of asymmetry in the mandibular body, rami, and condyles may hamper the accurate reconstruction of the resected areas. Shape estimation using SSM can address both of these limitations. Shape estimation through SSM is, therefore, a promising approach that could make it possible to treat a larger variety of pathologies and should be considered for inclusion in the future versions of the developed workflow.

The implants used in this study were designed in the shape of a cage. Even though several case studies have produced successful clinical outcomes with reconstruction implants in the shape of a cage or tray, there are some potential disadvantages to construction with a cage and bone grafts. In particular, there are significant risks of bone resorption, wound dehiscence, extraoral implant exposure, and postoperative infection, leading to partial or total loss of the construction (Tideman et al., 1998; Kumar et al., 2016). This applies mainly to the patients who require the resection of malignant tumors together with a substantial amount of soft tissue. The approach used in this study could, nevertheless, be applied to patients who suffer from benign defects and those who have not (yet) been radiated, and to the situations where soft tissues are compromised only to a limited extent. To minimize the risks of infection and prevent contamination through the oral cavity, a two-stage intervention may be desirable. In such a scenario, first the resection is performed in combination with plate fixation. After healing, reconstruction can take place through the neck. It is important to realize that the application of the workflow proposed in this study is not limited to the design of cages. The workflow could also be used to create patient-specific reconstruction plates or any desired implant geometries for that matter. Since a mandible analog was used here, future studies should apply the developed workflow to actual patient cases.

4.2. FEA and experimental validation

The mechanical behavior of the materials involved in our analyses were simplified in various ways to reduce the complexity of the FEA models. Firstly, bone was modeled as an isotropic material even though bone is known to behave anisotropically. Secondly, all the materials present in our FEA models were assumed to be linear elastic while it is known that bone is a viscoelastic material (Lakes et al., 1979) and that highly porous lattice structures may experience localized plastic deformation even when the effective stress is well below the yield stress of the architected material (Benedetti et al., 2021). Finally, stress relaxation, hardening effects, and load redistributions that typically occur during dynamic loading are not considered in our FEA models. Because of these and other modeling simplifications, some discrepancies may be present between the absolute stress values obtained with FEA and the experimentally derived values, especially in the case of large deformations. The PU material used in the experiments is isotropic. It was, therefore, modeled correctly in the *EXP-FEA* model. To minimize the effects of plasticity on the predictions of the FEA models, the results of *EXP-FEA* were compared with the experimental data only within the linear elastic range of the associated force-displacement curves.

The elastic modulus of the PU mandible cortex in *EXP-FEA* was determined such that there was a good correspondence between the computational and experimental results. The selected value of the elastic modulus (0.41 GPa) was close to the value adopted by Koper et al. (2021), who used the same synthetic mandible analog and estimated its elastic modulus with the elastic modulus of standard PU (0.50 GPa). In this study, experimental tests were performed on PU mandible specimen, and hence homogeneous material assignment with cortical PU properties was sufficient for the validation of the computational models. Density values and elastic moduli were translated to those of the actual bone for the *PHY-FEA* models to predict clinical scenarios accurately. The material properties in the latter case were scaled to those of the actual bone based on the grey values obtained from the CT images. The number of materials chosen to describe the cancellous and cortical bone may not be sufficient to reflect the variations in the material properties of the actual mandibular bone. In fact, the number of materials could theoretically be reduced to two, considering the way the mandibles are manufactured with two distinct regions of cancellous bone and cortical bone. However, a more diverse spread of *HU* values was obtained from the CT images, indicating that some transition regions between the cancellous bone and cortical bone may have existed as well as some higher-density areas in the cortical region. In the case of actual clinical applications, the material properties of the bone (*i.e.*, density and elastic modulus) will be obtained from the *HU* values of each patient's CT images. The correlation between the *HU* values and bone density can be established either by imaging hydroxyapatite phantoms or be derived from the average bone density data available in the literature. As for the mechanical properties, the empirical relationships available in the literature between the bone density and elastic modulus (*e.g.*, Cheng et al. (2020); Kucukguven and Akkocaoğlu (2020)) could be employed. The patient-specific bone material properties would then be implemented in the FEA models to predict the mechanical and failure behaviors of both the bone and the entire construct.

Normally, a layer of periodontal ligament (PDL) is located between the tooth roots and the alveolar sockets, which is important for transferring the force to the alveolar bone. This very thin tissue cannot be easily captured with regular CT scanning protocols. Even though some other FEA studies have included this soft tissue layer between the teeth and the bone, it is often excluded from FEA models as it requires time-consuming manual segmentation steps and increases the processing time due to increased model complexity (Gröning et al., 2012). Several studies have, however, found that FEA models show a much higher stiffness and, thus, lower strains when teeth and bone are modeled as continuous objects as opposed to models where the PDL is included (Gröning et al., 2012; Marinescu et al., 2005). It is, therefore, suggested that future studies perform a sensitivity analysis to determine the effect of PDL on the accuracy of the FEA model predictions.

The regions associated with the high values of the von Mises stress (Fig. 6a) correspond well with the primary locations of failure observed during the mechanical tests, namely the condylar neck region. This suggests that the boundary conditions and forces are correctly implemented in the computational models. The compressive strength of the PU foam with densities between 0.240 and 0.641 g/cm^3 ranges between 4.7 and 24.7 MPa (Calvert et al., 2010). A maximum stress of 16 MPa observed in the FE model (condylar neck region) falls within this range, assuming that the cortical PU is of high enough density. The agreement between the deformation patterns shown in Fig. 7b and d indicates the correct implementation of the muscle force vector directions and the relative muscle force magnitudes. The good agreement in the stress patterns observed between Fig. 7a and c and those reported by Pinheiro and Alves (2015) indicates that the muscle forces are correctly scaled.

In all the three implant models, the condylar neck on the contralateral side is stressed the most during INC whereas the condylar neck on the lateral side is stressed the most during RMB. This observation agrees well with the quasi-static testing results (Fig. 9a and b) where the

fracture under the INC loading conditions consistently occurred in the contralateral condyle. Under the RMB loading conditions, the fracture always occurred in the lateral condyle. While the stress levels on the contralateral side of the mandible are comparable in the three implant models, the stress levels on the lateral side of the mandible seem to increase as the stiffness of the implant decreases. The resistance of the implanted mandible to deformation depends on the stiffness of the implant. With a lower implant stiffness, the resistance to the deformation must be smaller. The equivalent stresses will, consequently, be higher in the bone surrounding the implant. The maximum stresses on the implants can be found just below the first screw hole near the posterior resection margin. The area of the mandibular angle, especially the area around the screws close to the proximal resection margin, is known to represent a weak spot in reconstruction plates (Gutwald et al., 2017; Yi et al., 1999; Trainotti et al., 2014; Schupp et al., 2007).

The maximum and minimum principal strain values were extracted from two regions on the outer surface edges of the bone. When the surface on the outer edges is curved, the subtended angle of the camera view with respect to the sample will play an important role. As the curvature on the posterior surface of the condylar neck (Polygon_2) is relatively blunt, the back of the condylar neck may not be fully captured by the cameras (Fig. 5d). Since the strain values are expected to be the largest in that area, it may be the case that Polygon_2 covers a region with lower maximum strain values than those covered by Area_2 in the FE model, which could explain the offset in the principal strain values in Fig. 6-f. At the curved boundaries peak strains could be underestimated due to averaging errors given that the accuracy of the measurements depends on the pixel subset size used for the strain calculations (Chanda et al., 2015). Placing the cameras closer to the normal of the surfaces at the strain peak regions may improve the accuracy. Finally, a limitation regarding the comparison of the DIC measurements with the FEA results is that we only used one intact sample for DIC measurements. Comparing FEA with averaged DIC data from multiple specimens and taken at various camera angles may reduce the margin of error.

It is very challenging to mimic the *in vivo* three-dimensional loading configuration of the mandible. Simplifications are, therefore, needed. Seebach et al. (2018) showed that the biting forces could be described by a resultant vector originating from the mandibular angles. This approach was translated into the current setup by applying uniaxial forces that act on both mandibular angles (Fontana et al., 2016; Gateno et al., 2013; Rendenbach et al., 2017; Schupp et al., 2007; Koper et al., 2021). The various translational and rotational degrees of freedom integrated into the stage and the tooth supports of the experimental setup (Fig. 4a) make it possible to test intact and reconstructed mandibles with different sizes and shapes and under almost any desired loading conditions. This is particularly useful if cadaveric studies are going to be performed. The muscle forces acting on the reconstructed side are often reduced to some extent, leading to an unequal distribution of biting forces between both sides (Curtis et al., 1999; Marunick et al., 1992). In the present study, the muscles that could not retain their function after reconstruction were removed from the FE model, whereas in the experimental setup this loading imbalance was accounted for by distributing 70% and 30% of the total forces on the healthy and affected side, respectively (Schupp et al., 2007). It is important to mention is that this force distribution was selected because no reliable data could be found in the literature.

Two different methods were used to test the biomechanical performance of the reconstruction systems under cyclic loading, namely, the constant-cyclic-method and increment-cyclic-method. Methods like the former have been used by Schupp et al. (2007) and Wu et al. (2017), while the latter method was applied by Gateno et al. (2013) and Rendenbach et al. (2017). The fact that none of the implants failed during the quasi-static tests, either through fracture or screw/implant loosening, at loads far exceeding the maximal physiological biting forces indicates that the reconstruction was stable. The fatigue tests performed with the constant-cyclic-method indicated that the reconstruction systems performed very well at least up to 250.000 cycles at relatively high chewing forces. The high resistance of the reconstruction systems to mechanical failure was also confirmed by the absence of fatigue failure in the osteosynthesis during the tests with the increment-cyclic-method. The reason that sample 2 in the TO-implant group fractured at a different location during the test with the increment-cyclic-method than the other specimens did was most likely minor manufacturing defects (cavities), which were observed at several locations along the fracture line.

A limitation regarding the data analysis approach can be identified. The fact that no large differences in the stiffness, ultimate load, or ultimate displacement were observed between the implanted and intact mandibles suggests that both implants will perform well in taking over the function of the original bone segment. This might also indicate that there is still a margin to further increase the porosity inside the implants. However, the low sample size per loading condition in the tests can be seen as a limitation, as it reduces the statistical power. Due to budget constraints, the sample sizes were minimized and determined such that the validation of the computational models could be established and the potentially (significant) differences between the two implant designs could still be revealed. Random sampling was applied within and between the experimental groups. All the samples were prepared in an identical fashion, followed by randomly allocating them to each of the experimental groups and random testing them for each loading condition. The variations between the specimens were minimized by using one type of mandible model, using a surgical guide for sample preparation, and ensuring an identical positioning of the samples during the mechanical tests. The level of variations within each group was, therefore, limited, making it safer to draw conclusions on the significance of the relative differences between the groups despite the low sample sizes. A Kruskal-Wallis non-parametric test ($p < 0.05$) with Bonferroni correction was performed to investigate the effects of any potential deviations from a normal distribution on the results of the performed statistical analysis. The results of the non-parametric test regarding statistical significance, however, matched those of the parametric *t*-test (*i.e.,* no significant differences in stiffness, ultimate load, or ultimate displacement were found between both implant designs).

Since the mechanical performances of the LA- and TO-implants were not found to be significantly different, the LA-implant may be preferrable to the TO implant for clinical application due to the four following reasons. First, the weight of the LA-implant is slightly lower than that of the TO-implant, which will increase the patient comfort while reducing the material costs. Second, the LA-implant has a higher porosity, which is likely to result in a higher degree of osseointegration and bone tissue regeneration (Schouman et al., 2016; Zhou et al., 2010). Third, the increased porosity presumably leads to a lower implant stiffness, which is beneficial for reducing stress shielding. Finally, the relatively time-consuming TO process (18 h for the implant designed here, excluding the additional post-processing time) can be omitted.

5. Conclusions

We demonstrated the capability of the proposed workflow to design and analyze patient-specific mandibular reconstruction cage implants with excellently reproduced mandibular contours and high resistance to mechanical failure. The proposed workflow will, after future incorporation of an FEA plugin, provide surgeons and medical engineers with a systematic approach and the tools to design and evaluate patient-specific reconstruction implants. This would enable cost- and time-effective pre-surgical planning and the design of customized implants that can maximize the aesthetic and functional outcomes while minimizing the associated morbidities.

CRediT authorship contribution statement

A. van Kootwijk: Conceptualization, Data curation, Formal analysis,

Investigation, Methodology, Software, Validation, Visualization, Writing – original draft. **V. Moosabeiki:** Writing – review & editing, Visualization, Supervision, Methodology, Investigation. **M. Cruz Saldivar:** Investigation. **H. Pahlavani:** Software. **M.A. Leeflang:** Investigation, Methodology. **S. Kazemivand Niar:** Investigation. **P. Pellikaan:** Conceptualization, Supervision. **B.P. Jonker:** Writing – review & editing, Resources, Conceptualization. **S.M. Ahmadi:** Conceptualization, Resources, Supervision, Writing – review & editing. **E.B. Wolvius:** Writing – review & editing, Supervision, Resources, Conceptualization. **N. Tümer:** Conceptualization, Investigation, Methodology, Supervision, Writing – review & editing. **M.J. Mirzaali:** Writing – review & editing, Supervision, Project administration, Methodology, Investigation, Conceptualization. **J. Zhou:** Funding acquisition, Writing – review & editing. **A.A. Zadpoor:** Writing – review & editing, Resources, Funding acquisition, Conceptualization.

Declaration of competing interest

The authors declare that they have no known competing financial interests or personal relationships that could have appeared to influence the work reported in this paper.

Acknowledgements

The work is part of the 3DMed project that has received funding from the Interreg 2 Seas programme 2014–2020, co-funded by the European Regional Development Fund under subsidy contract No. 2S04-014.

Appendix A. Supplementary data

Supplementary data to this article can be found online at https://doi.org/10.1016/j.jmbbm.2022.105291.

References

Ay, M., Kubat, T., Delilbasi, C., Ekici, B., Yuzbasioglu, H.E., Hartomacioglu, S., 2016. 3D Bio-Cad modeling of human mandible and fabrication by rapid-prototyping technology. Usak Univ. J. Mater. Sci. 2 (2), 135–145. https://doi.org/10.12748/uujms.201324255.

Benedetti, M., Du Plessis, A., Ritchie, R.O., Dallago, M., Razavi, S.M.J., Berto, F., 2021. Architected cellular materials: a review on their mechanical properties towards fatigue-tolerant design and fabrication. Mater. Sci. Eng. R Rep. 144, 100606 https://doi.org/10.1016/j.mser.2021.100606.

Bobbert, F.S.L., Zadpoor, A.A., 2017. Effects of bone substitute architecture and surface properties on cell response, angiogenesis, and structure of new bone. J. Mater. Chem. B 5 (31), 6175–6192. https://doi.org/10.1039/C7TB00741H.

Calvert, K.L., Trumble, K.P., Webster, T.J., Kirkpatrick, L.A., 2010. Characterization of commercial rigid polyurethane foams used as bone analogs for implant testing. J. Mater. Sci. Mater. Med. 21 (5), 1453–1461. https://doi.org/10.1007/s10856-010-4024-6.

Chanda, S., Dickinson, A., Gupta, S., Browne, M., 2015. Full-field in vitro measurements and in silico predictions of strain shielding in the implanted femur after total hip arthroplasty. Proc. Inst. Mech. Eng. H 229 (8), 549–559. https://doi.org/10.1177/0954411915591617.

Cheng, K., Liu, Y., Yao, C., Zhao, W., Xu, X., 2019. A personalized mandibular implant with supporting and porous structures designed with topology optimization - a case study of canine. Rapid Prototyp. J. 25 (2), 417–426. https://doi.org/10.1108/RPJ-11-2017-0231.

Cheng, K.J., Liu, Y.F., Wang, R., Zhang, J.X., Jiang, X.F., Dong, X.T., Xu, X., 2020. Topological optimization of 3D printed bone analog with PEKK for surgical mandibular reconstruction. J. Mech. Behav. Biomed. Mater. 107, 103758 https://doi.org/10.1016/j.jmbbm.2020.103758.

Coletti, D.P., Ord, R., Liu, X., 2009. Mandibular reconstruction and second generation locking reconstruction plates: outcome of 110 patients. Int. J. Oral Maxillofac. Surg. 38 (9), 960–963. https://doi.org/10.1016/j.ijom.2009.03.721.

Curtis, D.A., Plesh, O., Hannam, A.G., Sharma, A., Curtis, T.A., 1999. Modeling of jaw biomechanics in the reconstructed mandibulectomy patient. J. Prosthet. Dent 81 (2), 167–173. https://doi.org/10.1016/s0022-3913(99)70244-1.

Doty, J.M., Pienkowski, D., Goltz, M., Haug, R.H., Valentino, J., Arosarena, O.A., 2004. Biomechanical evaluation of fixation techniques for bridging segmental mandibular defects. Arch. Otolaryngol. Head Neck Surg. 130 (12), 1388–1392. https://doi.org/10.1001/archotol.130.12.1388.

Ettl, T., Driemel, O., Dresp, B.V., Reichert, T.E., Reuther, J., Pistner, H., 2010. Feasibility of alloplastic mandibular reconstruction in patients following removal of oral squamous cell carcinoma. J. Cranio-Maxillo-Fac. Surg. 38 (5), 350–354. https://doi.org/10.1016/j.jcms.2009.04.011.

Fontana, S.C., Smith, R.B., Nazir, N., Andrews, B.T., 2016. Biomechanical assessment of fixation methods for segmental mandible reconstruction with fibula in the polyurethane model. Microsurgery 36 (4), 330–333. https://doi.org/10.1002/micr.30052.

Gateno, J., Cookston, C., Hsu, S.S., Stal, D.N., Durrani, S.K., Gold, J., Ismaily, S., Alexander, J.W., Noble, P.C., Xia, J.J., 2013. Biomechanical evaluation of a new MatrixMandible plating system on cadaver mandibles. J. Oral Maxillofac. Surg. 71 (11), 1900–1914. https://doi.org/10.1016/j.joms.2013.06.218.

Goh, B.T., Lee, S., Tideman, H., Stoelinga, P.J., 2008. Mandibular reconstruction in adults: a review. Int. J. Oral Maxillofac. Surg. 37 (7), 597–605. https://doi.org/10.1016/j.ijom.2008.03.002.

Gröning, F., Fagan, M., O'Higgins, P., 2012. Modeling the human mandible under masticatory loads: Which input variables are important? Anat Rec (Hoboken) 295 (5), 853–863. https://doi.org/10.1002/ar.22455.

Gutwald, R., Jaeger, R., Lambers, F.M., 2017. Customized mandibular reconstruction plates improve mechanical performance in a mandibular reconstruction model. Comput. Methods Biomech. Biomed. Eng. 20 (4), 426–435. https://doi.org/10.1080/10255842.2016.1240788.

Kakarala, K., Shnayder, Y., Tsue, T.T., Girod, D.A., 2018. Mandibular reconstruction. Oral Oncol. 77, 111–117. https://doi.org/10.1016/j.oraloncology.2017.12.020.

Khalifa, G.A., Abd El Moniem, N.A., Elsayed, S.A., Qadry, Y., 2016. Segmental mirroring: does it eliminate the need for intraoperative readjustment of the virtually pre-bent reconstruction plates and is it economically valuable? J. Oral Maxillofac. Surg. 74 (3), 621–630. https://doi.org/10.1016/j.joms.2015.09.036.

Kondo, S., Katsuta, H., Akizuki, A., Kurihara, Y., Kamatani, T., Yaso, A., Nagasaki, M., Shimane, T., Shirota, T., 2015. Computer-assisted surgery for mandibular reconstruction using a patient-specific titanium mesh tray and particulate cancellous bone and marrow. Case Rep. Clin. Med. 4, 85–92. https://doi.org/10.4236/crcm.2015.43019.

Koper, D.C., Leung, C.A.W., Smeets, L.C.P., Laeven, P.F.J., Tuijthof, G.J.M., Kessler, P.A. W.H., 2021. Topology optimization of a mandibular reconstruction plate and biomechanical validation. J. Mech. Behav. Biomed. Mater. 113, 104157 https://doi.org/10.1016/j.jmbbm.2020.104157.

Korioth, T.W., Hannam, A.G., 1994. Deformation of the human mandible during simulated tooth clenching. J. Dent. Res. 73 (1), 56–66. https://doi.org/10.1177/00220345940730010801.

Koschwanez, H.E., Reichert, W.M., 2013. Textured and porous materials. In: Biomaterials Science: an Introduction to Materials, third ed. Elsevier, pp. 321–331.

Kucukguven, M.B., Akkocaoğlu, M., 2020. Finite element analysis of stress distribution on reconstructed mandibular models for autogenous bone grafts. Technol. Health Care 28 (3), 249–258. https://doi.org/10.3233/THC-191809.

Kumar, B.P., Venkatesh, V., Kumar, K.A., Yadav, B.Y., Mohan, S.R., 2016. Mandibular reconstruction: overview. J. Maxillofac. Oral Surg. 15 (4), 425–441. https://doi.org/10.1007/s12663-015-0766-5.

Lakes, R.S., Katz, J.L., Sternstein, S.S., 1979. Viscoelastic properties of wet cortical bone–I. Torsional and biaxial studies. J. Biomech. 12 (9), 657–678. https://doi.org/10.1016/0021-9290(79)90016-2.

Lee, W.B., Choi, W.H., Lee, H.G., Choi, N.R., Hwang, D.S., Kim, U.K., 2018. Mandibular reconstruction with a ready-made type and a custom-made type titanium mesh after mandibular resection in patients with oral cancer. Maxillofac. Plast Reconstr. Surg. 40 (1), 35. https://doi.org/10.1186/s40902-018-0175-z.

Lee, Y.W., You, H.J., Jung, J.A., Kim, D.W., 2018. Mandibular reconstruction using customized three-dimensional titanium implant. Arch. Craniofac. Surg. 19 (2), 152–156. https://doi.org/10.7181/acfs.2018.01830. Epub 2018 Jun 20.

León, D.N., Flórez, G.M., Gualdrón, C.L., 2020. Low-cost mandibular reconstruction workflow. Oral Maxillofac. Surg. Cases 6 (2), 100146. https://doi.org/10.1016/j.omsc.2020.100146.

Li, C.H., Wu, C.H., Lin, C.L., 2020. Design of a patient-specific mandible reconstruction implant with dental prosthesis for metal 3D printing using integrated weighted topology optimization and finite element analysis. J. Mech. Behav. Biomed. Mater. 105, 103700 https://doi.org/10.1016/j.jmbbm.2020.103700.

Liu, Y.F., Fan, Y.Y., Jiang, X.F., Baur, D.A., 2017. A customized fixation plate with novel structure designed by topological optimization for mandibular angle fracture based on finite element analysis. Biomed. Eng. Online 16 (1), 131. https://doi.org/10.1186/s12938-017-0422-z.

Liu, Y.F., Zhu, F.D., Dong, X.T., Peng, W., 2011. Digital design of scaffold for mandibular defect repair based on tissue engineering. J. Zhejiang Univ. - Sci. B 12 (9), 769–779. https://doi.org/10.1631/jzus.B1000323.

Malekpour, Z., Sarkarat, F., Hooshangi, H., 2014. Mandibular reconstruction using custom-made titanium mesh tray and autogenous bone graft: a case report. Thrita 3 (4), e22291. https://doi.org/10.5812/thrita.22291.

Marinescu, R., Daegling, D.J., Rapoff, A.J., 2005. Finite-element modeling of the anthropoid mandible: the effects of altered boundary conditions. Anat Rec. A Discov. Mol. Cell Evol. Biol. 283 (2), 300–309. https://doi.org/10.1002/ar.a.20166.

Marunick, M.T., Mathes, B.E., Klein, B.B., 1992. Masticatory function in hemimandibulectomy patients. J. Oral Rehabil. 19 (3), 289–295. https://doi.org/10.1111/j.1365-2842.1992.tb01104.x.

Merema, B.B.J., Kraeima, J., Glas, H.H., Spijkervet, F.K.L., Witjes, M.J.H., 2021. Patient-specific finite element models of the human mandible: lack of consensus on current set-ups. Oral Dis. 27 (1), 42–51. https://doi.org/10.1111/odi.13381.

Moghaddam, N.S., Jahadakbar, A., Amerinatanzi, A., Elahinia, M., Miller, M., Dean, D., 2016. Metallic fixation of mandibular segmental defects: graft immobilization and orofacial functional maintenance. Plast. Reconstr. Surg. Glob. Open 4 (9), e858. https://doi.org/10.1097/GOX.0000000000000859.

Moiduddin, K., Al-Ahmari, A., Nasr, E.S.A., Al Kindi, M., Ramalingam, S., Kamrani, A., 2016. Comparing 3-Dimensional virtual reconstruction methods in customized implants. Int. J. Adv. Biotechnol. Res. 7 (1), 323–331.

Moiduddin, K., Mian, S.H., Ahmed, N., Ameen, W., Al-Khalefah, H., Mohammed, M.K., Umer, U., 2020. Integrative and multi-disciplinary framework for the 3D rehabilitation of large mandibular defects. Int. J. Adv. Manuf. Technol. 106, 3831–3847. https://doi.org/10.1007/s00170-019-04762-3.

Moiduddin, K., Mian, S.H., Alkhalefah, H., Umer, U., 2019. Digital design, analysis and 3D printing of prosthesis scaffolds for mandibular reconstruction. Metals 9 (5), 569. https://doi.org/10.3390/met9050569.

Mounir, M., Abou-ElFetouh, A., ElBeialy, W., Mounir, R., 2020. Patient-specific alloplastic endoprosthesis for reconstruction of the mandible following segmental resection: a case series. J. Cranio-Maxillo-Fac. Surg. 48 (8), 719–723. https://doi.org/10.1016/j.jcms.2020.06.006.

Nasr, E.A., Al-Ahmari, A.M., Moiduddin, K., Al Kindi, M., Kamrani, A.K., 2017. A digital design methodology for surgical planning and fabrication of customized mandible implants. Rapid Prototyp. J. 23 (1), 101–109. https://doi.org/10.1108/RPJ-11-2014-0157.

Oldhoff, M.G.E., Mirzaali, M.J., Tümer, N., Zhou, J., Zadpoor, A.A., 2021. Comparison in clinical performance of surgical guides for mandibular surgery and temporomandibular joint implants fabricated by additive manufacturing techniques. J. Mech. Behav. Biomed. Mater. 119 (2), 104512 https://doi.org/10.1016/j.jmbbm.2021.104512.

Paré, A., Bossard, A., Laure, B., Weiss, P., Gauthier, O., Corre, P., 2019. Reconstruction of segmental mandibular defects: Current procedures and perspectives. Laryngoscope Investig Otolaryngol 4 (6), 587–596. https://doi.org/10.1002/lio2.325.

Park, J.H., Odkhuu, M., Cho, S., Li, J., Park, B.Y., Kim, J.W., 2020. 3D-printed titanium implant with pre-mounted dental implants for mandible reconstruction: a case report. Maxillofac. Plast Reconstr. Surg. 42 (1), 28. https://doi.org/10.1186/s40902-020-00272-5.

Peng, W.M., Cheng, K.J., Liu, Y.F., Nizza, M., Baur, D.A., Jiang, X.F., Dong, X.T., 2021. Biomechanical and Mechanostat analysis of a titanium layered porous implant for mandibular reconstruction: the effect of the topology optimization design. Mater. Sci. Eng. C Mater. Biol. Appl. 124, 112056. https://doi.org/10.1016/j.msec.2021.112056.

Pinheiro, M., Alves, J.L., 2015. The feasibility of a custom-made endoprosthesis in mandibular reconstruction: implant design and finite element analysis. J. Cranio-Maxillo-Fac. Surg. 43 (10), 2116–2128. https://doi.org/10.1016/j.jcms.2015.10.004.

Qassemyar, Q., Assouly, N., Temam, S., Kolb, F., 2017. Use of a three-dimensional custom-made porous titanium prosthesis for mandibular body reconstruction. Int. J. Oral Maxillofac. Surg. 46 (10), 1248–1251. https://doi.org/10.1016/j.ijom.2017.06.001.

Rachmiel, A., Shilo, D., Blanc, O., Emodi, O., 2017. Reconstruction of complex mandibular defects using integrated dental custom-made titanium implants. Br. J. Oral Maxillofac. Surg. 55 (4), 425–427. https://doi.org/10.1016/j.bjoms.2017.01.006.

Radwan, D., Mobarak, F., 2018. Plate-related complications after mandibular reconstruction: observational study osteotomy. Egypt. J. Oral Maxillofac. Surg. 9 (1), 22–27. https://doi.org/10.21608/OMX.2018.5623.

Rendenbach, C., Sellenschloh, K., Gerbig, L., Morlock, M.M., Beck-Broichsitter, B., Smeets, R., Heiland, M., Huber, G., Hanken, H., 2017. CAD-CAM plates versus conventional fixation plates for primary mandibular reconstruction: a biomechanical in vitro analysis. J. Cranio-Maxillo-Fac. Surg. 45 (11), 1878–1883. https://doi.org/10.1016/j.jcms.2017.08.024.

Schouman, T., Schmitt, M., Adam, C., Dubois, G., Rouch, P., 2016. Influence of the overall stiffness of a load--bearing porous titanium implant on bone ingrowth in critical--size mandibular bone defects in sheep. J Mech Behav Biomed Mater 59, 484–496. https://doi.org/10.1016/j.jmbbm.2016.02.036.

Schupp, W., Arzdorf, M., Linke, B., Gutwald, R., 2007. Biomechanical testing of different osteosynthesis systems for segmental resection of the mandible. J. Oral Maxillofac. Surg. 65 (5), 924–930. https://doi.org/10.1016/j.joms.2006.06.306.

Seebach, M., Theurer, F., Foehr, P., Deimling, C., Burgkart, R., Zaeh, M.F., 2018. Design of bone plates for mandibular reconstruction using topology and shape optimization. Adv. Struct. Multidiscip. Optim. 2086–2096. https://doi.org/10.1007/978-3-319-67988-4_154.

Seol, G.J., Jeon, E.G., Lee, J.S., Choi, S.Y., Kim, J.W., Kwon, T.G., Paeng, J.Y., 2014. Reconstruction plates used in the surgery for mandibular discontinuity defect. J. Kor. Assoc. Oral Maxillofac. Surg. 40 (6), 266–271. https://doi.org/10.5125/jkaoms.2014.40.6.266.

Shibahara, T., Noma, H., Furuya, Y., Takaki, R., 2002. Fracture of mandibular reconstruction plates used after tumor resection. J. Oral Maxillofac. Surg. 60 (2), 182–185. https://doi.org/10.1053/joms.2002.29817.

SLM Solutions, Material Data Sheet. https://www.slm-solutions.com/fileadmin/Content/Powder/MDS/MDS_Ti-Alloy_Ti6Al4V_ELI_0719_EN.pdf (accessed 10 April 2021).

Tideman, H., Samman, N., Cheung, L.K., 1998. Functional reconstruction of the mandible: a modified titanium mesh system. Int. J. Oral Maxillofac. Surg. 27 (5), 339–345. https://doi.org/10.1016/s0901-5027(98)80061-1.

Trainotti, S., Raith, S., Kesting, M., Eichhorn, S., Bauer, F., Kolk, A., Lethaus, B., Hölzle, F., Steiner, T., 2014. Locking versus nonlocking plates in mandibular reconstruction with fibular graft–a biomechanical ex vivo study. Clin. Oral Invest. 18 (4), 1291–1298. https://doi.org/10.1007/s00784-013-1105-1.

van Eijden, T.M., 2000. Biomechanics of the mandible. Crit. Rev. Oral Biol. Med. 11 (1), 123–136. https://doi.org/10.1177/10454411000110010101.

Vignesh, U., Mehrotra, D., Howlader, D., Singh, P.K., Gupta, S., 2019. Patient specific three- dimensional implant for reconstruction of complex mandibular defect. J. Craniofac. Surg. 30 (4), e308–e311. https://doi.org/10.1097/SCS.0000000000005228.

Wang, Z., Wang, C., Li, C., Qin, Y., Zhong, L., Chen, B., Li, Z., Liu, H., Chang, F., Wang, J., 2017. Analysis of factors influencing bone ingrowth into three-dimensional printed porous metal scaffolds: a review. J. Alloys Compd. 717, 271–285. https://doi.org/10.1016/j.jallcom.2017.05.079.

Wong, R.C., Tideman, H., Merkx, M.A., Jansen, J., Goh, S.M., Liao, K., 2011. Review of biomechanical models used in studying the biomechanics of reconstructed mandibles. Int. J. Oral Maxillofac. Surg. 40 (4), 393–400. https://doi.org/10.1016/j.ijom.2010.11.023.

Wu, C.H., Lin, Y.S., Liu, Y.S., Lin, C.L., 2017. Biomechanical evaluation of a novel hybrid reconstruction plate for mandible segmental defects: a finite element analysis and fatigue testing. J. Cranio-Maxillo-Fac. Surg. 45 (10), 1671–1680. https://doi.org/10.1016/j.jcms.2017.07.010.

Yamashita, Y., Yamaguchi, Y., Tsuji, M., Shigematsu, M., Goto, M., 2008. Mandibular reconstruction using autologous iliac bone and titanium mesh reinforced by laser welding for implant placement. Int. J. Oral Maxillofac. Implants 23 (6), 1143–1146.

Yi, Z., Jian-Guo, Z., Guang-Yan, Y., Ling, L., Fu-Yun, Z., Guo-Cheng, Z., 1999. Reconstruction plates to bridge mandibular defects: a clinical and experimental investigation in biomechanical aspects. Int. J. Oral Maxillofac. Surg. 28 (6), 445–450. https://doi.org/10.1016/S0901-5027(99)80058-7.

Zhou, L.B., Shang, H.T., He, L.S., Bo, B., Liu, G.C., Liu, Y.P., Zhao, J.L., 2010. Accurate reconstruction of discontinuous mandible using a reverse engineering/computer-aided design/rapid prototyping technique: a preliminary clinical study. J. Oral Maxillofac. Surg. 68 (9), 2115–2121. https://doi.org/10.1016/j.joms.2009.09.033.